[6] Watson, J., "On Spatially-Growing Finite Disturbances in Plane Poiseuille Flow," *Journal of Fluid Mechanics*, Vol. 14, 1962, pp. 211–221.

[7] Taylor, G. I., "Stability of a Viscous Liquid Contained Between Two Rotating Cylinders," *Philosophical Transactions of the Royal Society*, Vol. A223, 1923, pp. 289–343.

[8] Liu, J. T. C., "A General Theory of the Development of Finite-Amplitude Disturbances in the Unstable Laminar Wake Behind Plane Bodies at Hypersonic Speeds," AIAA Paper 68-684, Los Angeles, Calif., 1968.

[9] Ko, D. R. S., "Non-Linear Stability Theory for a Laminar, Incompressible Wake," Part II, Ph.D. thesis, 1969, California Inst. of Technology.

[10] Ko, D. R. S., Kubota, T., and Lees, L., "Finite Disturbance Effect on the Stability of a Laminar Incompressible Wake Behind a Flat Plate," *Journal of Fluid Mechanics*, Vol. 40, Pt. 2, 1970, pp. 315–341.

[11] Lin, C. C., "On Uniformly Valid Asymptotic Solutions of the Orr-Sommerfeld Equation," *Proceedings of the 9th International Congress of Applied Mechanics*, 1957, pp. 136–148.

[12] Lees, L. and Gold, H., "Stability of Laminar Boundary Layers and Wakes at Hypersonic Speeds. Part I. Stability of Laminar Wakes," *Proceedings of International Symposium of Fundamental Phenomena in Hypersonic Flow*, Cornell University Press, Ithaca, N.Y., 1966.

[13] Batchelor, G. K. and Gill, A. E., "Analysis of the Stability of Axisymmetric Jets," *Journal of Fluid Mechanics*, Vol. 14, 1962, pp. 529–551.

[14] Mack, L. M., "Computation of the Stability of the Laminar Boundary Layer," *Methods in Computational Physics*, Vol. 4, Academic Press, New York, 1965, pp. 247–299.

[15] Lees, L. and Hromas, L. A., "Turbulent Diffusion in the Wake of a Blunt-Nosed Body at Hypersonic Speeds," *Journal of the Aerospace Sciences*, Vol. 29, No. 8, Aug. 1962.

[16] Ohrenberger, J. T. and Baum, E., "A Theoretical Model of the Near Wake of a Slender Body in Supersonic Flow," AIAA Paper 70-792, Los Angeles, Calif., 1970.

[17] Batt, R. G., "Experimental Investigation of Wakes Behind Two-Dimensional Slender Bodies at $M = 6$," Ph.D. thesis, 1967, California Inst. of Technology.

SEPTEMBER 1971 AIAA JOURNAL VOL. 9, NO. 9

Aerodynamics of Slender Bodies and Wing-Body Combinations at $M_\infty = 1$

JOHN R. SPREITER*
Stanford University, Stanford, Calif.

AND

STEPHEN S. STAHARA†
Nielsen Engineering & Research Inc., Mountain View, Calif.

An account is given of recent theoretical results for steady inviscid transonic flows around a variety of three-dimensional bodies of aerodynamic interest. The local linearization method for axisymmetric flow is combined with the transonic equivalence rule to calculate pressure distributions for freestream Mach number one on the surface and in the near flowfield of a number of slender, pointed, axisymmetric and nonaxisymmetric bodies, including simple wing-body combinations, for both nonlifting and lifting conditions. Comparisons with experiment exhibit good agreement, except near the rear of some of the bodies, particularly those with maximum thickness far forward or on lifting bodies at larger angles of attack. It is suggested that the former is due primarily to wind-tunnel wall interference, and the latter to boundary-layer separation and vortex generation.

I. Introduction

THE purpose of this paper is to describe a theoretical procedure for determining the pressure distributions at freestream Mach number M_∞ equal unity on the surface and in the near flowfield of slender bodies and wing-body combinations, both nonlifting and lifting, and to demonstrate the quality of the results by comparison with experiment. The analysis is based on the small disturbance theory of inviscid transonic flow, and makes use of the approximations of slender-body theory, the transonic equivalence rule, and the method of local linearization for axisymmetric flow with $M_\infty = 1$. Results are presented for bodies of revolution having maximum diameter located between 30% and 70% of the body length, for parabolic-arc bodies of elliptic cross section, and for both a conical and a more general wing-body combination. Angles of attack α range from 0° to 6°. The examples were selected, insofar as possible, to enable comparison with existing data obtained either in a conventional transonic wind tunnel with partly open walls or in a solid-wall wind tunnel operating in the choked condition to simulate flow with $M_\infty = 1$.

Received June 15, 1970; presented as Paper 70-798 at the AIAA 3rd Fluid and Plasma Dynamics Conference, Los Angeles, Calif., June 29–July 1, 1970; revision received December 17, 1970. This work was supported by NASA/Ames Research Center under Contract NAS2-5410.

* Professor, Departments of Applied Mechanics and Aeronautics and Astronautics; also Consultant, Nielsen Engineering & Research Inc. Associate Fellow AIAA.

† Senior Research Scientist. Member AIAA.

II. Theory

Basic Equations

The analysis is expressed primarily in terms of a body-fixed Cartesian coordinate system centered at the nose with the x axis directed rearward and aligned with the longitudinal axis of the body, the y axis directed to the right, facing forward, and the z axis directed vertically upward, as illustrated in Fig. 1. The freestream direction may be inclined any small

angle to the x axis, although attention is confined to cases in which it is in the x-z plane, i.e., no sideslip. Because of the fundamental assumption of inviscid small disturbance theory that the flow is irrotational, the velocity $\mathbf{v}$ can be expressed as the gradient of a potential Φ, which may, in turn, be related to a perturbation velocity potential ϕ according to[1]

$$\Phi(x,y,z) = U_\infty(x + \alpha z) + \phi(x,y,z) \quad (1)$$

where U_∞ represents the freestream velocity. The partial differential equation for ϕ has been approximated by a variety of forms in transonic flow studies; but we use the following form for the reasons put forward in Ref. 2 and confirmed in subsequent studies.

$$(1 - M_\infty^2)\phi_{xx} + \phi_{yy} + \phi_{zz} = M_\infty^2[(\gamma + 1)/U_\infty]\phi_x\phi_{xx} \quad (2)$$

This equation applies whether the coordinate system is aligned with the x axis parallel to the direction of the freestream, as in most derivations,[2,3] or inclined a small angle to it as in the present applications to lifting configurations.[1] The expression for the pressure coefficient C_p is not invariant with respect to small rotations of the coordinate system, however, and is as follows in the aforementioned coordinate system[1]

$$C_p = \frac{p - p_\infty}{\rho_\infty U_\infty^2/2} = -\frac{2}{U_\infty}(\phi_x + \alpha\phi_z) - \frac{1}{U_\infty^2}(\phi_y^2 + \phi_z^2) \quad (3)$$

The boundary conditions require that $\mathbf{v} = \hat{\imath}U_\infty + \hat{k}\alpha U_\infty$ infinitely far from the body, where $\hat{\imath}$, $\hat{\jmath}$, and $\hat{k}$ are unit vectors parallel to the x, y, and z axes, and that the velocity component v_n normal to the body surface be zero at the body. The boundary conditions for ϕ for slender bodies or thin wings having small n_1 are then[1]

$$\phi(\infty) = 0,\ [U_\infty(n_1 + \alpha n_3) + n_2\phi_y + n_3\phi_z]_{\text{body}} = [U_\infty(n_1 + \alpha n_3) + \phi_n]_{\text{body}} = 0 \quad (4)$$

where $\hat{n} = \hat{\imath}n_1 + \hat{\jmath}n_2 + \hat{k}n_3$ is the unit normal to the surface, and n_1, n_2, and n_3 are the direction cosines of $\hat{n}$ with respect to the x, y, and z axes. Since attention will be confined to flows with $M_\infty = 1$ having all shock waves downstream of the region for which results will be calculated, we will not require the corresponding relation for conditions on the two sides of a shock wave. The preceding equations provide therefore the fundamental relations for the analysis to follow.

Transonic Equivalence Rule

The transonic equivalence rule first announced by Oswatitsch[4,5] for flow past thin nonlifting wings, and later extended to lifting wings[6] and slender bodies of arbitrary cross section,[1] provides a means for greatly simplifying the analysis of flow with $M_\infty = 1$ past a wide class of slender bodies, including wing-body combinations, for both nonlifting and lifting situations, by relating the flow around the slender body of arbitrary cross section to that past an "equivalent" nonlifting body of revolution having the same longitudinal distribution of cross section area $S(x)$. This rule is closely associated with the transonic area rule of Whitcomb[7] relating to drag, but pertains in addition to the properties of the flowfield, such as the velocity and pressure, that are derivable from a knowledge of the potential. It is also closely related to one of the simplest results of slender-body theory of subsonic and supersonic, as well as transonic, flow, which states that ϕ in the vicinity of a slender body of arbitrary cross section is approximately

$$\phi = \phi_2 + g(x) \quad (5)$$

where ϕ_2 is the solution of the two-dimensional Laplace's equation

$$\phi_{yy} + \phi_{zz} = 0 \quad (6)$$

for the given boundary conditions in the y-z plane at each x station, and $g(x)$ is an additional contribution dependent upon M_∞ and $S(x)$, but not on the shape of the cross section. It is thus possible to determine $g(x)$ from the solution of the simpler problem of axisymmetric flow at the same M_∞ past the equivalent body. Aside from the significant reductions of the transonic drag rise achieved by application of Whitcomb's area rule, the opportunities for advance provided by the transonic equivalence rule have never been fully exploited.

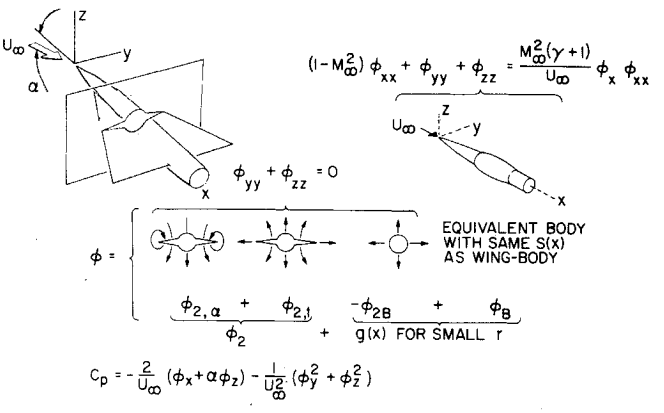

Fig. 1 Illustration of transonic equivalence rule.

It is advantageous to express the equivalence rule as

$$\phi = \phi_{2,\alpha} + \phi_{2,t} - \phi_{2,B} + \phi_B \quad (7)$$

in which each component of ϕ has the meaning indicated in Fig. 1. Equation (7) may be derived from Eq. (5) by writing $\phi = \phi_2 + g(x)$ for the body of arbitrary cross section and subtracting the corresponding expression for the equivalent body. The order of error in Eq. (7) has been established[1] for thin wings of aspect ratio A, chord c, and thickness ratio τ. It was found that the magnitude of the quantity $\phi/U_\infty c$ retained in the equivalence rule is $0(A\tau \ln A)$, whereas that of the quantities discarded in the derivation for $M_\infty = 1$ is $0(A^4\tau^2 \ln A)$. Since the magnitude of the quantities discarded in the derivation of the corresponding result in linearized subsonic and supersonic flow past slender bodies is $0(A^3\tau \ln A)$, it follows that the equivalence rule ought to be applicable to wings of greater aspect ratio at $M_\infty = 1$ than at any other Mach number.

Once ϕ is determined, the pressure distribution on or near a slender body is provided by Eq. (3). The results may be integrated to obtain the total forces, including lift and drag, and moments on slender bodies or wing-body combinations of arbitrary cross section. Since the aerodynamic loading, lift, and all lateral forces and moments may be expressed in terms of differences in pressure between pairs of points at the same longitudinal station, these quantities depend solely on ϕ_2 and are independent of M_∞. In particular, we note, as discussed long ago,[8,9] that these quantities may be calculated using a linearized slender-body theory even though $M_\infty = 1$.

Local Linearization Method for Axisymmetric Flow with $M_\infty = 1$

Approximate solutions of good accuracy for axisymmetric flow with $M_\infty = 1$ past a wide class of slender pointed bodies may be obtained by application of the method of local linearization.[10] This method was first developed for two-dimensional flow past thin airfoils,[11] and subsequently extended to three-dimensional flow past thin wings of finite span[12] (see Refs. 13 and 14 for comprehensive summaries). Without repeating details of the derivation, this method provides the following nonlinear ordinary differential equation for $u = \phi_x$ at $M_\infty = 1$ on that part of the surface of a slender

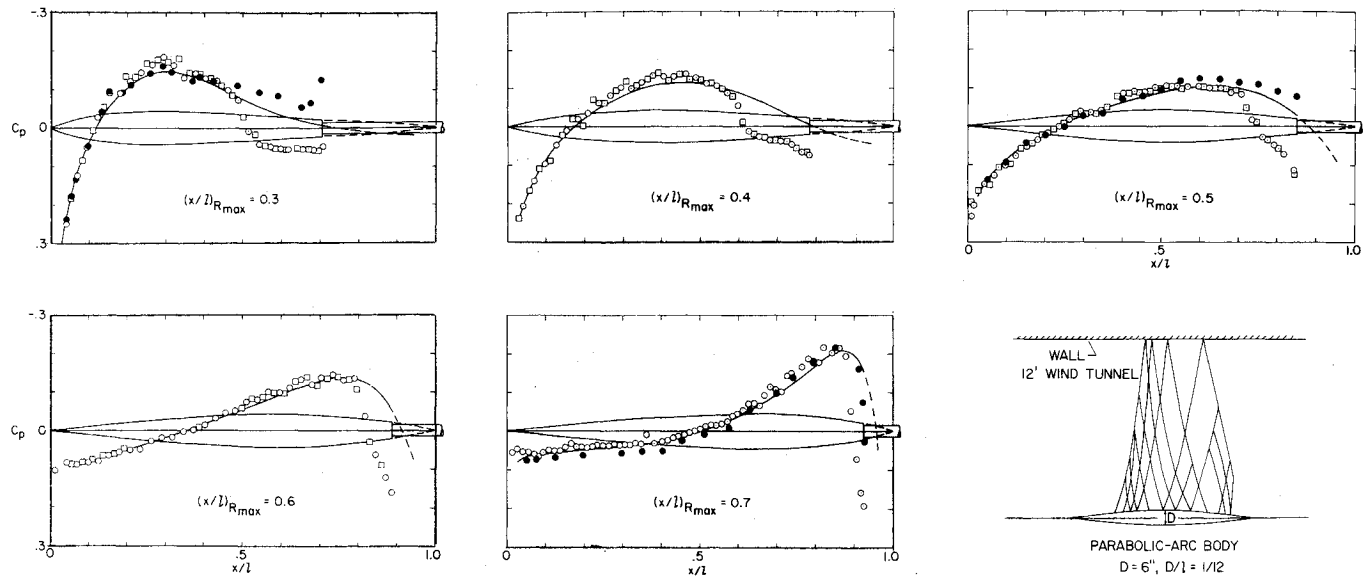

Fig. 2 Pressure distributions at $M_\infty = 1$ on five nonlifting bodies of revolution, and a plot of the theoretical characteristics network of the parabolic-arc body illustrating effects of the wind-tunnel walls. Open symbols represent data for 6-in. diam models in a 14-ft transonic wind tunnel,[16] closed symbols for data on same models in a choked 12-ft solid-wall wind tunnel.[15]

body of revolution along which $\partial u/\partial x > 0$:

$$\frac{u}{U_\infty} = \frac{S''(x)}{4\pi} \ln \left\{ \left[\frac{d}{dx}\left(\frac{u}{U_\infty}\right) - \frac{S'(x)S''(x)}{4\pi S(x)} \right] \times \frac{(\gamma+1)S(x)e^C}{4\pi x} \right\} + \frac{1}{4\pi}\int_0^x \frac{S''(x) - S''(\xi)}{x-\xi}\, d\xi \quad (8)$$

where $S = \pi R^2$ represents the cross section area, primes indicate differentiation with respect to x or ξ as indicated, C represents Euler's constant ≈ 0.5772, and

$$(d/dx)(u/U_\infty) - S'(x)S''(x)/4\pi S(x) = \partial u/U_\infty/\partial x \quad (9)$$

Equation (8) is useful for flows that are accelerating from subsonic to supersonic speeds, but must be supplemented by additional expressions that are valid for decelerating flows as well. Such equations were also derived in Ref. 10, and are as follows for $M_\infty = 1$:

$$\frac{d}{dx}\left(\frac{u}{U_\infty}\right) = \frac{S'''(x)}{4\pi} \ln\left[-\frac{(\gamma+1)u}{U_\infty}\right] + \frac{d}{dx}\left[\frac{S''(x)}{4\pi}\ln\frac{S(x)}{4\pi x(l-x)} + \frac{1}{4\pi}\int_0^l \frac{S''(x) - S''(\xi)}{x-\xi}\, d\xi\right] \quad (10)$$

for a region of locally subsonic flow (i.e., $u < 0$), and

$$\frac{d}{dx}\left(\frac{u}{U_\infty}\right) = \frac{S'''(x)}{4\pi} \ln\frac{(\gamma+1)u}{U_\infty} + \frac{d}{dx}\left[\frac{S''(x)}{4\pi}\ln\frac{S(x)}{4\pi x^2} + \frac{1}{2\pi}\int_0^x \frac{S''(x) - S''(\xi)}{x-\xi}\, d\xi\right] \quad (11)$$

for a region of locally supersonic flow (i.e., $u > 0$). Although Eqs. (10) and (11) are both for flows with $M_\infty = 1$, neither is useful for the transition from subsonic to supersonic flow because of the presence of the $\ln(-u)$ term in Eq. (10) and the $\ln u$ term in Eq. (11).

Application of the preceding equations requires the evaluation of a constant of integration. If the location of the sonic point is known, as for a cone-cylinder for which it is at the shoulder, the constant for Eq. (8) can be evaluated simply by requiring that $u = 0$ at that point. For a smoothly curved body, however, the location of the sonic point would ordinarily not be known in advance, nor would a value for u be known at any other point, except at the nose where the logarithmically infinite value for u indicated by slender-body theory renders the knowledge provided by stagnation conditions useless for the present purposes. A simple procedure that has been found to lead to satisfactory results in applications of Eq. (8) is to select the one and only integral curve that is analytic (all derivatives finite) at the point where $S''(x)$ vanishes. As shown in Ref. 10, this procedure suffices to determine a unique solution that is in good agreement with experimental data. Theoretically, it assures that the solution for u can be expanded in a Taylor's series in the neighborhood of the point where $S''(x) = 0$, and this in turn provides the starting values necessary to continue the calculation by application of standard numerical techniques. Further away from the sonic point, u may reach a maximum or minimum, and Eq. (8) would no longer be capable of providing a good representation of the flow. The solution for such regions may be determined by use of Eq. (10) if the flow is subsonic or Eq. (11) if the flow is supersonic, with the integration constant and point of connection with the solution of Eq. (8) selected so that both u and du/dx are continuous at that point. For further details, reference should be made to Ref. 10 and also to Ref. 11, where some analogous situations for two-dimensional flow past thin airfoils are discussed.

III. Results

Pressure Distributions on the Surface and in the Near Flowfield of Several Nonlifting Bodies

In the original presentation of the method of local linearization for axisymmetric flow,[10] the theory was applied to flow with $M_\infty = 1$ past slender cone-cylinders and parabolic-arc bodies of revolution, and the results were compared with data for several such bodies having various values for the diameter-length ratio D/l. In Ref. 15, similar results were given for two additional bodies of revolution having $D/l = \frac{1}{12}$, but with the locations of maximum diameter at 30% and 70% of the body length. The latter were part of a series of bodies of revolution tested in the Ames 14-ft transonic wind tunnel.[16] The ordinates of these bodies having maximum diameter at 50%, 60%, and 70% of the body length are given by

$$R/l = A[(x/l) - (x/l)^n] \quad (12)$$

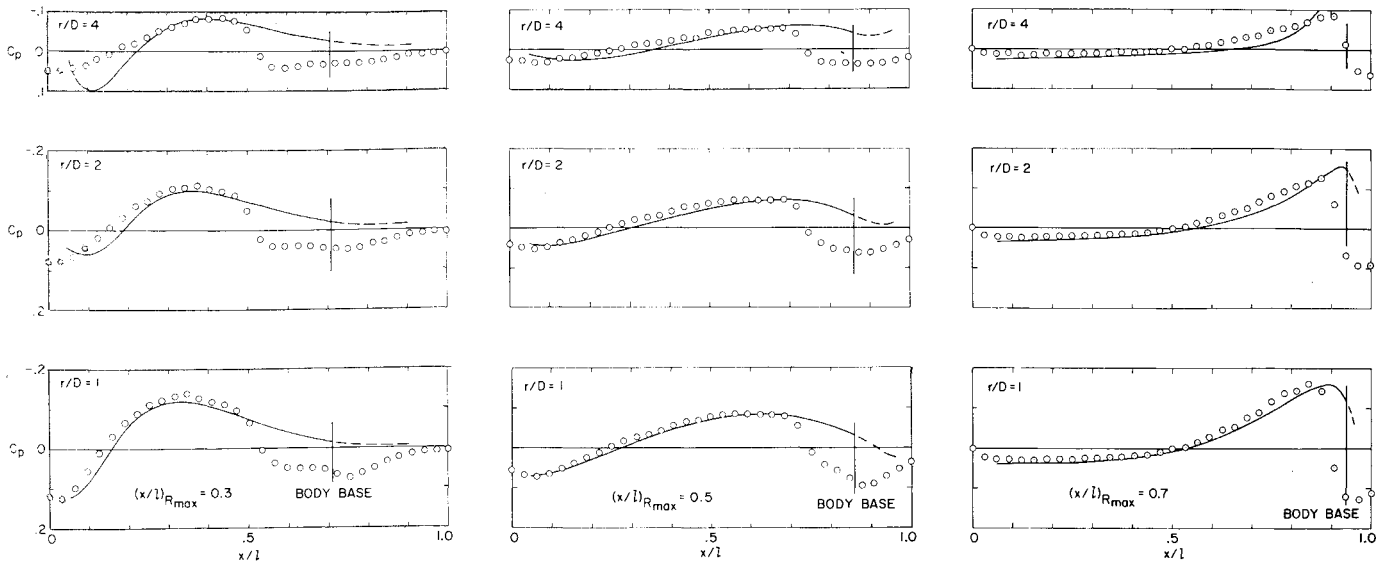

Fig. 3 Experimental[16] and theoretical pressure distributions at $M_\infty = 1$ in the flowfields of three of the bodies of revolution shown in Fig. 2.

with $n = 2.00$, 3.38, and 6.03, while the same values for n applied to

$$R/l = A[(1 - x/l) - (1 - x/l)^n] \tag{13}$$

provide the ordinates for those bodies with maximum diameter at 50%, 40%, and 30% of the length. In both Eqs. (12) and (13), A is related to D/l and n by

$$A = [n^{n/(n-1)}/2(n - 1)](D/l) \tag{14}$$

Figure 2 shows the experimental surface pressure distributions[15,16] for the five different bodies with $D/l = \frac{1}{12}$ together with the theoretical results calculated using the local linearization method. The theoretical results for the bodies with maximum diameter at 30%, 50%, and 70% of the body length have been given previously[10,15]; those for the bodies with maximum diameter at 40% and 60% of the body length are new and serve to complete the comparisons for the entire series of bodies tested. Also included on the plots for the bodies with maximum diameter at 30%, 50%, and 70% of the body lengths are a second set of experimental results[15] obtained when the models used in the original tests in the 14-ft transonic wind tunnel were tested in the Ames 12-ft pressure wind tunnel with solid walls under choked conditions to simulate flow with $M_\infty = 1$, as indicated to be appropriate by transonic flow theory. It may be seen that the pressure distributions calculated using the local linearization method are in essential agreement with the measurements in both wind tunnels over the forebodies, but that substantial discrepancies appear among the results for the afterbodies, particularly for the bodies with maximum thickness forward of the midpoint. As noted originally,[15] the data from the choked wind tunnel are generally on the opposite side of the theoretical curve from the data from the transonic wind tunnel.

With respect to the discrepancies on the afterbodies, many would dismiss further discussion by attributing the differences to shock-wave/boundary-layer interaction effects not included in the theory. While there is little doubt that such effects are important, the characteristic diagram in the lower right-hand part of Fig. 2 suggests that the discrepancies are due, at least in part, to wind-tunnel-wall interference. This diagram shows the characteristic lines for an unbounded flow with $M_\infty = 1$ past a parabolic-arc body of revolution with $D/l = \frac{1}{12}$. They have been calculated by applying the transonic similarity rule for axisymmetric flow[17] to a related diagram[18] calculated for a parabolic-arc body of revolution with $D/l = \frac{1}{6}$. The position of the wall with respect to a 6-in. diam model in the 12-ft pressure wind tunnel is as indicated, and the nearest part of the wall in the tests in the 14-ft transonic wind tunnel is $\frac{7}{6}$ as far away. Although it was thought at the time the tests in the 14-ft transonic wind tunnel were conducted that the 6 in. diam of the models was sufficiently small to avoid significant effects of wind-tunnel-wall interference, this diagram shows that such may not be the case because Mach waves originating from the forepart of the body are indicated to be reflected from the walls onto the aft part of the body. It can be seen, furthermore, that the most upstream reflected Mach wave strikes the body at about $x/l = 0.6$ in the 12-ft wind tunnel, and slightly aft of that location in the 14-ft wind tunnel. The effect of the reflected waves striking the body is to make the pressure coefficients more negative in the 12-ft wind tunnel, because the outgoing characteristics represent expansion waves that reflect from the solid wall of the tunnel as rarefaction waves. The effects are amplified, moreover, because of the focusing characteristics of the reflected axisymmetric waves as they collapse down onto a part of the body that has a smaller circumference than that from which they originated. The sign of the corresponding effects in the 14-ft transonic wind tunnel is not so simple to ascertain, but it appears that the reflections from the partly open wall of that wind tunnel are very nearly equal in magnitude, but opposite in sign, to the reflections from the solid wall of the 12-ft wind tunnel. In addition to the direct effects of the reflected waves impinging on the rear of the body, there exists the distinct possibility of significant augmentation arising from the interaction of the boundary layer with a shock wave that may form adjacent to the body. The latter may form either because of coalescence of compression waves reflecting from the body or because of boundary-layer separation resulting from the wall-induced steepening of the adverse pressure gradients. In either case, it is clear that considerable additional study will have to be made before it is possible to properly evaluate the significance of discrepancies between theoretical and experimental pressure distributions on the aft parts of slender bodies.

Once C_p has been determined for the body surface, it is a simple matter to calculate the pressure distribution throughout the near flowfield by using the expression

$$(C_p)_r = (C_p)_R - \frac{1}{\pi} S''(x) \ln\frac{r}{R} - \left[\frac{S'(x)}{2\pi}\right]^2 \left(\frac{1}{r^2} - \frac{1}{R^2}\right) \tag{15}$$

relating the pressure coefficient $(C_p)_r$ at an arbitrary, but small, distance r from the body axis to that $(C_p)_R$ at the body surface $r = R(x)$ at the same x location. This relation may

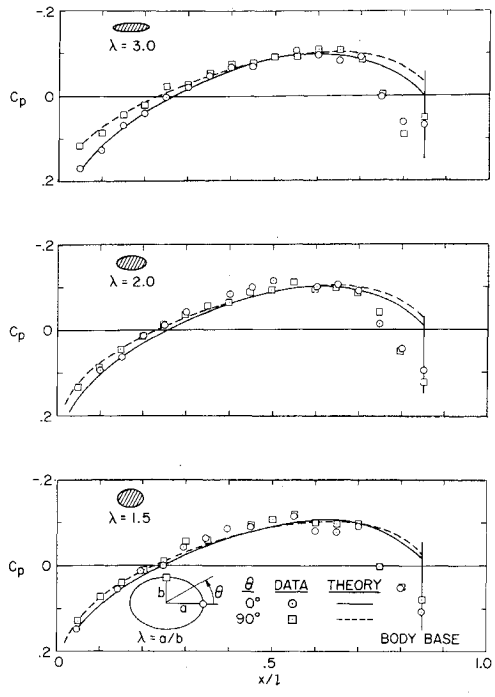

Fig. 4 Experimental[19] and theoretical pressure distributions at $M_\infty = 1$ along two lines on three nonlifting bodies having different elliptic cross sections.

be derived from Eqs. (3) and (5) with ϕ_2 given by

$$\phi_2 = (U_\infty/2\pi)(dS/dx) \ln r \qquad (16)$$

Figure 3 shows flowfield data from the Ames 14-ft transonic wind tunnel for several r/D for three of the bodies of Fig. 2 compared with the results calculated using Eq. (15) and the theoretical surface pressure distributions of Fig. 2 provided by the local linearization method. Except near the rear of the bodies where effects associated with the aforementioned discrepancies for the surface pressures are in evidence, the theoretical and experimental results are in satisfactory agreement for r/D as large as 4 for the 50% and 70% bodies, and at least 2 for the 30% body. Deterioration sets in with increasing r/D for any body because of the growing violation of the small r approximation of the theory, and is greatest for the 30% body because of the greater strain imposed on the slender-body approximations by the blunter nose of this body. Altogether, the comparisons indicate a wide region of applicability of the theory, particularly when considered with respect to possible applications of the transonic equivalence rule to configurations having wings or related extremities of such size that they, rather than the body, provide the major contribution to C_p at lateral distances of the order of those for which results are shown in Fig. 3.

As a first application of the transonic equivalence rule combined with the local linearization results for the surface pressure distribution on the equivalent body of revolution, we consider a family of bodies with elliptic cross sections tested in the Ames 14-ft transonic wind tunnel.[19] Figure 4 presents the pressure distributions measured along the extremities of the major and minor axes ($\theta = 0°$ and 90°) at $M_\infty = 1$ for three bodies having values of 1.5, 2.0, and 3.0 for the ratio $\lambda = a/b$ of major to minor axes of the elliptic cross section, and having the same longitudinal distribution of cross section area $S = \pi ab$ as the parabolic-arc body with $D/l = 1/12$ for which results are shown in Figs. 2 and 3. Also included are the corresponding pressure distributions calculated using the equivalence rule with $\phi_{2,t}$ given by[20]

$$\phi_{2,t} = \text{R.P.}\left[\frac{U_\infty S'(x)}{2\pi} \ln \frac{\sigma + (\sigma^2 + a^2 + b^2)^{1/2}}{2}\right] \qquad (17)$$

in which R.P. indicates the real part, $\sigma = y + iz = re^{i\theta}$, $\phi_{2,B}$ is given by the expression for ϕ_2 in Eq. (16), and C_p is related to ϕ by Eq. (3) with $\alpha = 0$. Although the method of local linearization does not provide values for ϕ_B directly, only a knowledge of $g'(x) = dg(x)/dx$ is required for the calculation of the pressure, and it may be determined from the surface pressure coefficient $(C_p)_B$ on the equivalent nonlifting body of revolution by application of the following relation derived from Eqs. (3, 5, 7, and 16) (Ref. 1):

$$g'(x) = -(U_\infty/2)\{(C_p)_B + [S''(x)/2\pi] \ln(S/\pi) + S'^2(x)/4\pi S\} \qquad (18)$$

As in the previous comparisons, the theoretical and experimental results are in good agreement except near the rear of the bodies, where at least part of the discrepancies must be attributed to the extraneous effects of the wind-tunnel walls. Perhaps the most striking feature of the results shown on Fig. 4 is the smallness of the effects of the ellipticity of the cross section.

The corresponding results for the flowfield are shown in Fig. 5 for the body having $\lambda = 3$. As may be anticipated from the results of Fig. 4 for the surface pressures, the values for C_p at a given x are virtually independent of the azimuthal angle θ, and are, furthermore, very nearly identical to those shown in Fig. 3 at the same r/D for the equivalent body of revolution, namely, that with maximum diameter at 50% of the length. For these reasons, and in the interest of brevity, the flowfield results for the other two bodies of this series having smaller λ have been omitted.

Pressure Distributions on Lifting Bodies

As the first application to a lifting body, consider flow with $M_\infty = 1$ past the parabolic-arc body of revolution with $D/l = \frac{1}{12}$ for which the results for zero angle of attack are shown in Fig. 2. Experimental results for this body obtained in the Ames 14-ft transonic wind tunnel[19] at angles of attack $\alpha = 2°$, 4°, and 6° are shown in Figure 6 for three lines along the surface of the body, namely $\theta = 0°$ and $\pm 90°$. Also included on those plots are pressure distributions calculated

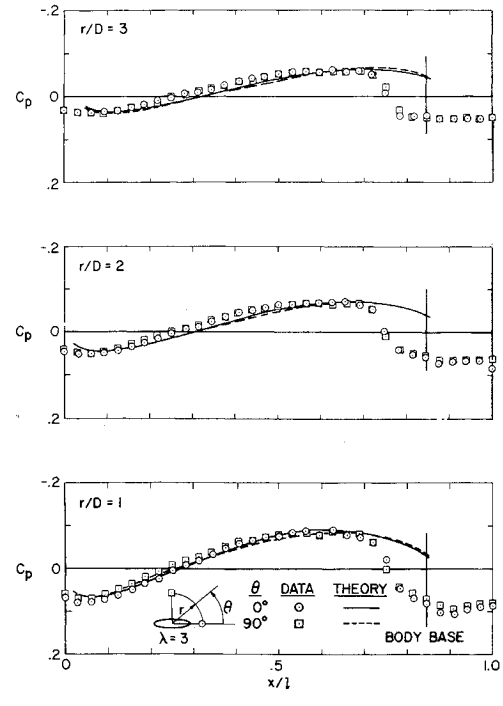

Fig. 5 Experimental[19] and theoretical pressure distributions at $M_\infty = 1$ in the flowfield of a nonlifting body having elliptic cross section.

using the transonic equivalence rule with $\phi_{2,\alpha}$ given by

$$\phi_{2,\alpha} = U_\infty \alpha S \sin\theta/\pi r \tag{19}$$

$\phi_{2,B}$ given by Eq. (16), $g'(x)$ by Eq. (18), and C_p by Eq. (3); all evaluated for the body having ordinates $R(x)$ given by Eq. (12) with $n = 2$. It may be seen that the agreement is good along most of the length of the body, and that significant discrepancies occur over the rear part of the body, much as in the case of the nonlifting bodies. The similarity of the comparisons, particularly at the smaller angles of attack, to those for $\alpha = 0°$ shown in Fig. 2 lend support to the idea that wind-tunnel wall interference effects are significantly affecting the results along the rear of the body. The variation with θ of the differences between the theoretical and experimental pressures that becomes increasingly evident as α is increased to 6° suggests that additional effects having a nonaxisymmetric character are present along the aft portion of the body. Although we can cite no definitive supporting evidence from these tests, we are inclined to conjecture that the experimental results are beginning to be influenced by vortex separation caused by the crossflow velocity component, as is familiar at both subsonic and supersonic speeds.

Similar comparisons of theoretical and experimental results for lifting bodies of elliptic cross section in flow with $M_\infty = 1$ are shown in Figs. 7 and 8 for a pair of bodies having values of 2 and 3 for the ratio a/b of major to minor axes. Both bodies have the same longitudinal distribution of cross section as the parabolic-arc body of $D/l = \frac{1}{12}$ for which results are shown in Figs. 2 and 6. The experimental results were obtained in tests in the Ames 14-ft transonic wind tunnel,[19] and are thus directly comparable to those presented in Figs. 2 and 6 for the parabolic-arc body of revolution tested in that wind tunnel. The theoretical results are calculated by using the transonic equivalence rule with $\phi_{2,\alpha}$ given by the following expression for two-dimensional potential flow about a body of elliptic cross section moving through still air with velocity $U_\infty\alpha$ (Ref. 20)

$$\phi_{2,\alpha} = \text{R.P.} \left\{ \frac{iU_\infty\alpha}{2} \left[\sigma - (\sigma^2 - a^2 + b^2)^{1/2} + \frac{a^2 + b^2}{\sigma + (\sigma^2 - a^2 + b^2)^{1/2}} \right] \right\} \tag{20}$$

$\phi_{2,t}$ given by Eq. (17), C_p by Eq. (3), and $g'(x)$ by Eq. (18)

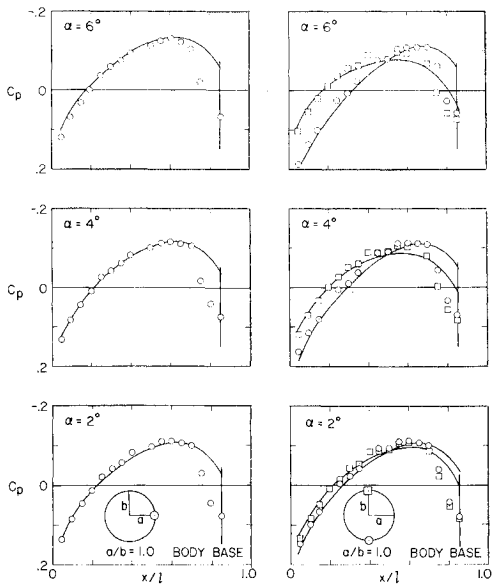

Fig. 6 Experimental[19] and theoretical pressure distributions at $M_\infty = 1$ along three lines on a lifting parabolic-arc body of revolution at three angles of attack.

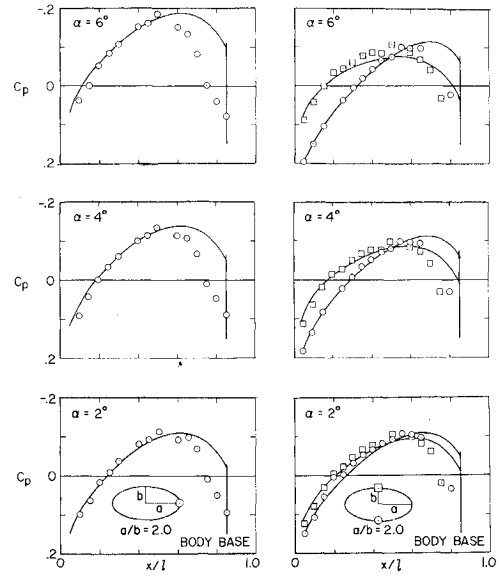

Fig. 7 Experimental[19] and theoretical pressure distributions at $M_\infty = 1$ along three lines on a lifting body having elliptic cross section with $a/b = 2$ at three angles of attack.

with values for $(C_p)_B$ provided by the method of local linearization. The comparisons show that the trends already described for the body of revolution are repeated; good agreement occurs along most of the length of each body, and notable deterioration sets in along the rear part. The observation that the discrepancies are most pronounced for the body with $a/b = 3$ and at 6° provides support for the suggestion that the experimental results for the rear of the lifting bodies are influenced by vortex separation at the larger angles of attack.

Pressure Distribution on Thin Wings and Slender Wing-Body Combinations

As we turn our attention toward wing-body combinations, it is instructive to recall the example of the thin cone-cylinder, or equivalently a cone of finite length, considered theoretically in Ref. 1, experimentally in Ref. 21, and summarized in Ref. 13. In general, the ordinates of the upper surface of the cone

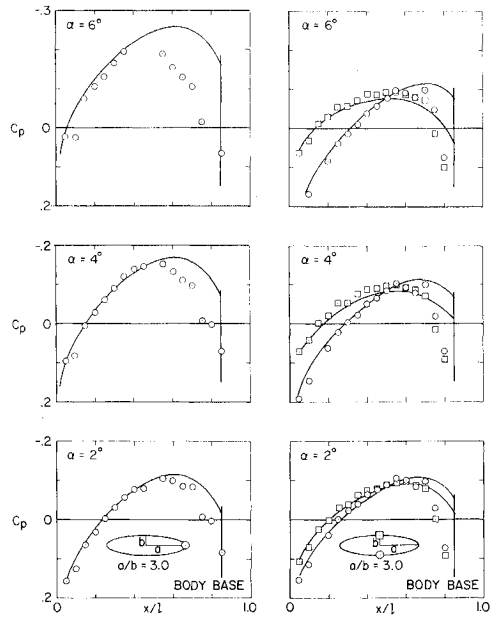

Fig. 8 Experimental[19] and theoretical pressure distributions at $M_\infty = 1$ along three lines on a lifting body having elliptic cross section with $a/b = 3$ at three angles of attack.

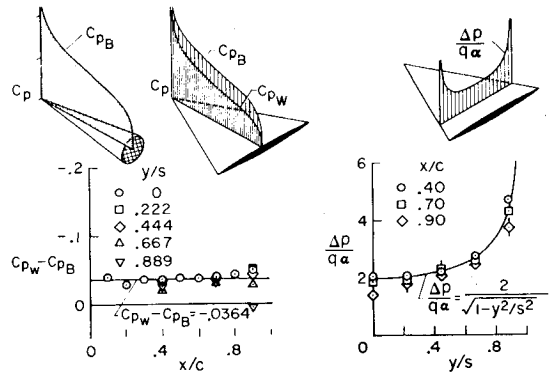

Fig. 9 Pressure distributions at $M_\infty = 1$ on a thin elliptic cone-cylinder and on the equivalent body of revolution.[13]

are given by

$$Z_u(x,y) = t(m^2x^2 - y^2)^{1/2}/2ml \tag{21}$$

where m is the tangent of the semiapex angle of the planform, l is the length of the cone, and t is the maximum thickness of the cone. The elliptic section in the plane $x = x_1$ thus has major and minor semiaxes $a = mx_1$ and $b = tx_1/2l$, and cross section area $S(x_1) = \pi ab = \pi tmx_1^2/2l$. Although the theory was developed generally, the pressure distribution has been measured for only one example, namely that defined by $m = \frac{1}{2}$ and $t/l = 0.06$. If we consider the cone to be a triangular wing, such values correspond to an aspect ratio of 2 and a thickness ratio of 0.06. The equivalent body of revolution is a slender cone with semiapex angle $\omega = (mt/2l)^{1/2}$, which in this instance is equal to 0.1225 rad or 7°. Equations (17) and (20) could be used for $\phi_{2,t}$ and $\phi_{2,\alpha}$, but it is much simpler for the calculation of the surface pressure distribution to adopt the usual practice of thin-wing theory and evaluate these quantities on the wing surface approximated to be at $z = 0$ and for $-mx \leq y \leq mx$. With the additional neglect of b^2 compared with a^2, $\phi_{2,t}$ and $\phi_{2,\alpha}$ may be approximated by

$$\phi_{2,t} = (U_\infty tmx/2l)\ln(mx/2),\quad \phi_{2,\alpha} = \pm U_\infty\alpha(m^2x^2 - y^2)^{1/2} \tag{22}$$

where the upper sign is to be used on the upper surface and the lower sign on the lower surface of the wing. With the introduction of the further approximation customary in wing theory that the pressure coefficient is given by

$$(C_p)_W = -(2/U_\infty)\partial\phi/\partial x \tag{23}$$

it was shown in Ref. 1 that

$$(C_p)_W = (C_p)_B - \frac{mt}{2l}\left(1 + \ln\frac{ml}{2t}\right) \mp \frac{2\alpha m^2 x}{(m^2x^2 - y^2)^{1/2}} \tag{24}$$

where the convention concerning upper and lower signs still holds, and $(C_p)_B$ represents the pressure distribution on the surface of the equivalent body, a circular cone-cylinder, at zero angle of attack. If the method of local linearization is used to determine the latter, we have that[10,13]

$$(C_p)_B = -2\omega^2\ln\frac{\omega x}{l} + \omega^2\ln\left\{\frac{16}{(\gamma+1)\omega e^C}\frac{x}{l}\times\left(1 - \frac{x}{l}\right)\right\} + \frac{\omega^2}{2}\left(\frac{1 - 3x/l}{1 - x/l}\right) - \omega^2 \tag{25a}$$

for $0 \leq x/l \leq \frac{1}{3}$, and

$$(C_p)_B = -2\omega^2\ln\frac{\omega x}{l} + \omega^2\ln\left\{\omega^2 + \frac{4[1 - x^2/l^2]}{(\gamma+1)\omega^2 e^C}\right\} - \omega^2 \tag{25b}$$

for $\frac{1}{3} \leq x/l \leq 1$.

Figure 9 shows sketches of the wing of $m = \frac{1}{2}$, $\tau = 0.06$, the equivalent body of revolution, the pressure distributions on each at zero angle of attack, and the aerodynamic loading or difference in pressure

$$\Delta p/q_\infty = (C_p)_{W,l} - (C_p)_{W,u}$$

on the two sides of the wing, where subscripts l and u denote the lower and upper sides of the wing. For these parameters

$$(C_p)_W - (C_p)_B = -0.0364 \tag{26}$$

for zero angle of attack, and

$$\frac{\Delta p}{q_\infty} = \frac{4\alpha m^2 x}{(m^2x^2 - y^2)^{1/2}} = \frac{2\alpha}{(1 - y^2/s^2)^{1/2}} \tag{27}$$

where $s = mx$ is the semispan at a distance x from the apex. These results are shown in the two plots of Fig. 9 to be in satisfactory agreement with the experimental data of Ref. 21.

From the preceding analysis and applications, it is but a short step to the simple wing-body combinations of Figs. 10 and 11. In both examples, a flat plate triangular wing of zero thickness is combined with a slender body of revolution. In Fig. 10, the body is a slender cone with its apex at the nose of the wing. In Fig. 11, it is a truncated parabolic-arc body of revolution attached to the wing in such a way that the wing root extends from 25 to 75% of the complete body length. In order to relate the results most directly to those discussed above, the aspect ratio of the wing is taken to be 2, the semiapex angle of the conical body to be 7°, and the diameter-length ratio D/l of the complete parabolic-arc body to be $\frac{1}{12}$. At zero angle of attack, the wing does not affect the flow, and the pressure distribution is the same as on the surface, or at the corresponding point in the flowfield, of the isolated body as illustrated in the left parts of these figures. The pressure distribution at zero angle on the body of the conical wing-body combination is thus given by Eq. (25), and that on the wing at a distance r from the axis and x from the apex, as measured along the axis, is given by Eq. (15) with $S(x) = \pi R^2 = \pi\omega^2x^2$. No comparable analytic expressions can be cited for the pressure distribution on the second wing-body combination at zero angle of attack, illustrated in the left part of Fig. 11, but the results are the same as indicated in Figs. 2 and 3 for the corresponding points on the body surface and in the surrounding flow.

The aerodynamic loadings shown in the right parts of Figs. 10 and 11 have been computed using Eq. (3) for C_p, Eq. (7) for ϕ, Eq. (16) for $\phi_{2,t}$, and the following expression from Refs. 8 and 22 for $\phi_{2,\alpha}$:

$$\phi_{2,\alpha} = \pm\frac{U_\infty\alpha}{2^{1/2}}\left\{\left[-\left(1 + \frac{a^4}{r^4}\right)r^2\cos 2\theta + s^2\left(1 + \frac{a^4}{s^4}\right)\right] + \left[r^4\left(1 - \frac{a^4}{r^4}\right) + 4a^4\cos^2 2\theta + s^4\left(1 + \frac{a^4}{s^4}\right)^2 - 2s^2\left(1 + \frac{a^4}{r^4}\right)\left(1 + \frac{a^4}{s^4}\right)r^2\cos 2\theta\right]^{1/2}\right\}^{1/2} - U_\infty\alpha z \tag{28}$$

in which the sign is positive for the upper half-plane $0 \leq \theta \leq \pi$ and negative for the lower half-plane $\pi \leq \theta \leq 2\pi$, and where $a = a(x)$ and $s = s(x)$ represent the local radius of the

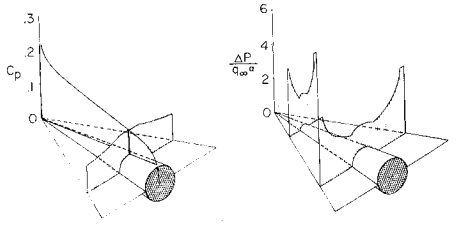

Fig. 10 Theoretical pressure distributions for $M_\infty = 1$ on a conical wing-body combination.

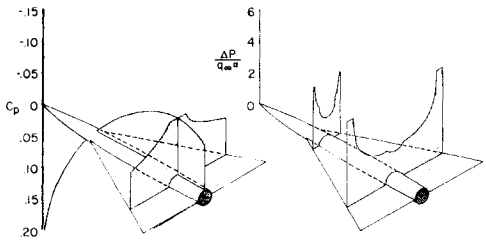

Fig. 11 Theoretical pressure distributions for $M_\infty = 1$ on a wing-body combination having a flat-plate triangular wing and a parabolic-arc body of revolution.

body and the semispan of the wing. For the specific examples just described

$$a = \omega x = 0.1225x;\ s = mx = x/2 \tag{29}$$

for the conical wing-body combination; and

$$a = 2D(x/l - x^2/l^2) = \tfrac{1}{6}(x/l - x/l^2) \tag{30a}$$

$$s = (l/2)(x/l - \tfrac{1}{4} + 3D/4l) = (l/2)(x/l - \tfrac{3}{16}) \tag{30b}$$

for the wing-body combination with the parabolic-arc body. Upon carrying out the indicated operations, the following expressions are found for the aerodynamic loading:

$$\frac{\Delta p}{q_\infty} = \frac{4\alpha\left\{\left[\frac{ds}{dx}\left(1 - \frac{a^4}{s^4}\right) + \frac{a}{s}\frac{da}{dx}\left(\frac{a^2}{s^2} - 1\right) + \left(1 - \frac{a^2}{y^2}\right)^2\right]\right\}}{[1 + a^4/s^4 - (y^2/s^2)(1 + a^4/y^4)]^{1/2}} \tag{31a}$$

on the wing, and

$$\frac{\Delta p}{q_\infty} = \frac{\left\{4\alpha\left[\frac{ds}{dx}\left(1 - \frac{a^4}{s^4}\right) + 2\frac{a}{s}\frac{da}{dx}\left(\frac{a^2}{s^2} + 1 - 2\frac{y^2}{a^2}\right)\right]\right\}}{[(1 + a^2/s^2)^2 - 4y^2/s^2]^{1/2}} \tag{31b}$$

on the body. Although we are unaware of any experimental data with which these or related results may be compared, the generally good agreement displayed in the preceding comparisons of pressure distributions on the bodies and wings separately suggests that correspondingly good agreement is to be anticipated for the wing-body combinations.

IV. Conclusion

In conclusion, we emphasize that the procedures by which these solutions have been obtained are not restricted to the particular examples selected for display in this paper, but possess much greater generality. Furthermore, the quality of the agreement with experimental results is sufficiently good, particularly when consideration is given to the numerous shortcomings inherent in transonic wind-tunnel testing, that we may go forward to more complicated configurations with confidence that the analysis is not only possible to carry out, but that the results will be of sufficient accuracy to be useful to aerodynamicists.

References

[1] Heaslet, M. A. and Spreiter, J. R., "Three-Dimensional Transonic Flow Theory Applied to Slender Wings and Bodies," Rept. 1318, 1957, NACA.

[2] Spreiter, J. R., "On the Application of Transonic Similarity Rules to Wings of Finite Span," Rept. 1153, 1953, NACA.

[3] Liepmann, H. W. and Roshko, A., *Elements of Gasdynamics*, Wiley, New York, 1957, pp. 202–205.

[4] Oswatitsch, K., "Die theoretischen Arbeiten über schallnahe Strömungen am Flugtechnischen Institut der Kungl. Tekniska Höskolan, Stockholm," *Eighth International Congress on Theoretical and Applied Mechanics*, Istanbul, 1952 (1953), pp. 261–262.

[5] Oswatitsch, K., "The Area Rule," *Applied Mechanics Reviews*, Vol. 10, No. 12, Dec. 1957, pp. 543–545.

[6] Spreiter, J. R., "Theoretical and Experimental Analysis of Transonic Flow Fields," *NACA-University Conference on Aerodynamics, Construction, and Propulsion II, "Aerodynamics,"* 1954, pp. 18-1–18-17.

[7] Whitcomb, R. T., "A Study of the Zero-Lift Drag-Rise Characteristics of Wing-Body Combinations Near the Speed of Sound," Rept. 1273, 1957, NACA.

[8] Spreiter, J. R., "The Aerodynamic Forces on Slender Plane- and Cruciform-Wing and Body Combinations," Rept. 962, 1950, NACA.

[9] Heaslet, M. A., Lomax, H., and Spreiter, J. R., "Linearized Compressible-Flow Theory for Sonic Flight Speeds," Rept. 956, 1950, NACA.

[10] Spreiter, J. R. and Alksne, A., "Slender Body Theory Based on Approximate Solution of the Transonic Flow Equation," TR R-2, 1959, NASA.

[11] Spreiter, J. R. and Alksne, A., "Thin Airfoil Theory Based on Approximate Solution of the Transonic Flow Equation," Rept. 1359, 1958, NACA.

[12] Alksne, A. and Spreiter, J. R., "Theoretical Pressure Distributions on Wings of Finite Span at Zero Incidence for Mach Numbers Near 1," TR R-88, 1961, NASA.

[13] Spreiter, J. R., "Aerodynamics of Wings and Bodies at Transonic Speeds," *Journal of the Aerospace Sciences*, Vol. 26, No. 8, Aug. 1959, pp. 465–487.

[14] Spreiter, J. R., "The Local Linearization Method in Transonic Flow Theory," *Symposium Transsonicum*, edited by K. Oswatitsch, Springer-Verlag, Berlin/Göttingen/Heidelberg, 1964, pp. 152–183.

[15] Spreiter, J. R., Smith, D. W., and Hyett, B. J., "A Study of the Simulation of Flow with Free-Stream Mach Number 1 in a Chocked Wind Tunnel," TR R-73, 1960, NASA.

[16] McDevitt, J. B. and Taylor, R. A., "Pressure Distributions at Transonic Speeds for Slender Bodies Having Various Axial Locations of Maximum Diameter," TN 4280, 1958, NACA.

[17] Oswatitsch, K. and Berndt, S. B., "Aerodynamic Similarity at Axisymmetric Transonic Flow Around Slender Bodies," KTH Aero TN 15, 1950, Royal Institute of Technology, Stockholm, Sweden.

[18] Oswatitsch, K., "Die Berechnung wirbelfreier achsensymmetrischer Überschallfelder," *Österreichisches Ingenieur-Archiv*, Band X, Heft 4, 1956, pp. 359–382.

[19] McDevitt, J. B. and Taylor, R. A., "Force and Pressure Measurements at Transonic Speeds for Several Bodies Having Elliptical Cross Sections," TN 4362, 1958, NACA.

[20] Nielsen, J. N., *Missile Aerodynamics*, McGraw-Hill, New York, 1960, p. 30.

[21] Page, W. A., "Experimental Study of the Equivalence of Transonic Flow About Slender Cone-Cylinders of Circular and Elliptic Cross Section," TN 4233, 1958, NACA.

[22] Spreiter, J. R. and Sacks, A. H., "A Theoretical Study of the Aerodynamics of Slender Cruciform-Wing Arrangements and Their Wakes," Rept. 1296, 1957, NACA.